

A Combined Level Set/Mesh Warping Algorithm for Tracking Brain and Cerebrospinal Fluid Evolution in Hydrocephalic Patients

Jeonghyung Park, Suzanne M. Shontz, and Corina S. Drapaca

Abstract Hydrocephalus is a neurological disease which occurs when normal cerebrospinal fluid (CSF) circulation is impeded within the cranial cavity. As a result, the brain ventricles enlarge, and the tissue compresses, causing physical and mental problems. Treatment has been mainly through CSF flow diversion by surgically implanting a CSF shunt in the brain ventricles or by performing an endoscopic third ventriculostomy (ETV). However, the patient response to either treatment continues to be poor. Therefore, there is an urgent need to design better therapy protocols for hydrocephalus. An important step in this direction is the development of predictive computational models of the mechanics of hydrocephalic brains. In this paper, we propose a combined level set/mesh warping algorithm to track the evolution of the ventricles in the hydrocephalic brain. Our combined level set/mesh warping method is successfully used to track the evolution of the brain ventricles in two hydrocephalic patients.

1 Introduction

Hydrocephalus (also called water on the brain) is a serious neurological disorder which occurs when normal cerebrospinal fluid (CSF) circulation is impeded within the cranial cavity. If hydrocephalus develops in infancy, the intracranial pressure is raised, and, as the CSF accumulates in the ventricles, the brain tissue compresses, and both the ventricles and the skull expand. The most common cause of infantile hydrocephalus in the U.S. is hemorrhage in the neonatal period, particularly in

Jeonghyung Park
The Pennsylvania State University, University Park, PA, 16802, e-mail: jxp975@cse.psu.edu

Suzanne M. Shontz
The Pennsylvania State University, University Park, PA, 16802, e-mail: shontz@cse.psu.edu

Corina S. Drapaca
The Pennsylvania State University, University Park, PA, 16802, e-mail: csd12@psu.edu

premature infants [13]. With approximately four million births occurring annually in the U.S., it is estimated that about 20%-74% of the approximately 50,000 very-low-birth-weight infants born yearly will develop post-hemorrhagic hydrocephalus. On the other hand, in the Sub-Saharan Africa which has one of the world's greatest disease burdens of bacterial meningitis, post-infections hydrocephalus is the most common form of infantile hydrocephalus with more than 100,000 cases arising each year.

The treatment of hydrocephalus is based on CSF flow diversion. The dilation of the ventricles can be reversed by either CSF shunt implantation or by performing an endoscopic third ventriculostomy (ETV) surgery, resulting in a relief from the symptoms of hydrocephalus. Despite the technical advances in shunt technology and endoscopy, the two treatment options display no statistically significant difference in the efficacy for treating hydrocephalus [83]. Endoscopic third ventriculostomy works well only in appropriately selected clinical cases of hydrocephalus [11], whereas shunt failure occurs in over 60% of patients [29]. Considering that many shunt recipients are children, and that shunts are lifelong commitments, these statistics underscore the importance of improving therapy. Furthermore, the postoperative persistence of the ventricular dilation constitutes a diagnostic limit for verifying the adequate functioning of ventriculostomy procedures in comparison with the treatment based on the placement of CSF shunt devices [13]. Therefore, there is an earnest need to design better therapy protocols for hydrocephalus.

An important step in this direction is the development of predictive mathematical and computational models of the mechanics of hydrocephalic brains. Many mathematical models have been proposed to explore the pathophysiology of hydrocephalus. The Monro-Kellie hypothesis [34, 49] simplifies the dynamics of the cranium to an underlying competition for space between CSF, blood, and brain parenchyma. This idea leads to numerous pressure-volume models where the CSF is contained within one compartment surrounded by compliant walls representing the brain parenchyma. These time-dependent models [16, 42, 78] (and references therein) are incapable of representing the complex dynamics of the cranium and provide little insight towards a more fundamental understanding of the development of hydrocephalus. Hakim [23] introduced a mechanical model describing the brain parenchyma as a porous sponge of viscoelastic material that compressed due to a pressure gradient causing the sponge cells to collapse. Nagashima [51] extended this model by applying Biot's theory of consolidation [7] and carried out simulations of the resulting mathematical model using the finite element method. This introduced one of the two current approaches to modeling the biomechanics of the brain parenchyma, namely the poroelastic model [32, 59, 79, 82, 84], in which the brain is considered to be a porous linearly elastic sponge saturated in a viscous incompressible fluid. These models account for the interaction of CSF with the brain parenchyma and thus can be used to model long-time scale phenomena such as the development of hydrocephalus. The second main approach is to model the brain parenchyma as a linear viscoelastic material [44, 45, 46, 88, 90]. Both linear viscoelastic and poroelastic models are based on the assumption of small strain theory which means that they are capable of predicting only small deformations. To cor-

rectly model the large deformations seen in hydrocephalus, nonlinear material laws are required and such models for brain parenchyma have been recently proposed in [14, 21]. These models are able to successfully predict the large ventricular displacements seen in hydrocephalus. However, most of the above mentioned mechanical models suffer from the assumption that the brain's geometry is either a cylinder or a sphere.

In order for mechanical models of brain to be of clinical relevance their corresponding computational algorithms and software must incorporate the anatomical geometry of the brain as seen in medical images as well as efficient and robust numerical solvers. Therefore, the aim of our paper is to propose an elegant computational approach that combines medical image processing, level set methods and moving meshes to simulate the mechanical behavior of hydrocephalic brains to treatments.

We propose a computational pipeline approach for evolution of the brain ventricles involving the following steps: image denoising, image segmentation based a threshold method, prediction of the ventricular boundaries via the level set method, generation of computational meshes of the brain, mesh deformation based using the finite element-based mesh warping (FEMWARP) method, and mesh quality improvement of the deformed meshes.

We review the literature in these areas in Section 2. We give a general introduction to level set methods and mesh warping methods and describe the specific methods being used in our combined level set/mesh warping approach in Section 3. Our computational pipeline approach for tracking the evolution of the brain ventricles is given in Section 4. Simulation results for the evolution of the brain ventricles in hydrocephalic patients post-treatment via shunt insertion are reported in Section 5. Section 6 explains our conclusions and future research plans.

2 Generation of Dynamic Biomedical Computational Models and Simulations

2.1 Generation of Image-Based Computational Models

Biomedical computational models which are derived from images are often created by following a specific pipeline approach [12]: (1) image processing (2) surface/volume mesh generation. Dynamic computational models also require the inclusion of a third step, i.e., (3) mesh motion. We highlight several of the existing techniques in these four areas found in the literature. A comprehensive review is not the focus of this section, as the literature is extensive; hence, we focus on the most similar approaches to the proposed approaches.

2.2 Image Segmentation

The image segmentation problem [64] is to partition an image into nonoverlapping regions whose union is the entire image; each identified region shares a characteristic such as image intensity or texture [24, 22, 56]. For segmentation of the image, it is also important that each region be connected. (Pixel classification [35] is a related problem whereby the constraint that each region be connected is removed. Although this can sometimes be desirable in medical image analysis, we seek to determine a classical segmentation of the image into regions as opposed to a discrete, pixel classification segmentation.) In medical image segmentation, each region would ideally represent an anatomical structure.

There are numerous image segmentation techniques available to researchers today. Popular approaches for medical image segmentation [64, 91, 40] include: thresholding methods (e.g., [66]), region growing methods (e.g., [27] and [28]), classifier methods from pattern recognition (e.g., [6] and [2]), clustering methods (e.g., [6]), Markov random field model methods (e.g., [25]), artificial neural network approaches (e.g., [41]), deformable models (e.g., [33, 43, 68]), and atlas-guided approaches (e.g., [19, 69]).

Level-set methods (e.g., [68, 53, 54, 48, 1, 17, 52, 60, 87]) represent one very popular deformable model approach that have been used extensively for image segmentation and for other image processing problems, such as image registration. In particular, the level set approach delineates region boundaries using closed parametric curves (or surfaces) that deform under the influence of a PDE; the problem is cast as a front evolution problem. This front propagation approach is different from the earlier energy minimization evolution approaches, such as snakes (e.g., [33, 43]). The speed of the deformation is essential to the position of the final contours. Local curvature of the contour, intensity gradient, shape, and position contours have all been used for the speed term [68]. One important advantage of level set methods is they permit easier handling of topological changes.

2.3 Mesh Generation

The classical approach for generating computational meshes from images that have been segmented and registered has been to perform a surface interpolation between the contours describing the segmented volume [18, 65, 67]. Often this is done using the marching cubes (MC) algorithm [39]. However, the regularized marching tetrahedron (RMT) algorithm [39] yields topologically-consistent surface meshes, whereas the MC method does not.

Computational biomedical meshes with tetrahedral [12, 20, 30, 81, 94, 37] or hexahedral [47, 70, 86, 95] elements are typically created for finite element or finite volume simulations based on the surface mesh input. Hybrid meshes [15, 58, 93] have also been used when high accuracy is required but hexahedral mesh generation is infeasible due to biomedical data complexity. Another possibility is to generate

a mesh based on the input of a level set [9]. Mesh optimization methods are used to improve the quality of biomedical meshes [26, 38, 85]; only recently have such techniques been designed for hybrid meshes [15].

2.4 Moving Meshes

Persson *et al.* [61, 63, 62, 80] developed a moving mesh technique based on the incorporation of level sets into an adaptive mesh refinement technique. They applied their moving mesh technique to image-based problems [61, 62]. Despite the fact that their applications involved a mesh, their algorithm does not compute the motion based upon the mesh; rather the motion is computed based upon the use of a Cartesian or octree background mesh and adaptive mesh refinement for mesh density control.

Mesh warping algorithms compute the deformation of the mesh from the source to the target domain based upon interpolation and/or extrapolation of the vertex coordinates. Typically the topology of the mesh is held fixed in order to allow for seamless integration with a numerical partial differential equation solver. Several mesh warping techniques for biomedical applications have been developed [3, 5, 36, 75, 76, 77]. However, they cannot be used for the development of computational models for tracking the evolution of the brain ventricles for hydrocephalus, as they do not incorporate the physics of the brain deformation due to the disease or its treatment.

Despite all of the research that has been performed in the areas of image processing, level sets, and dynamic mesh generation, there is no algorithm or software package which combines level sets with mesh warping. In addition, no such algorithms have been developed for tracking the evolution of the brain ventricles pre- and post-treatment of hydrocephalus.

3 Introduction to the Level Set Method and FEMWARP

In this section, we give an introduction to level set methods and mesh warping methods for applications with deforming domains. In addition, we describe the specific level set and mesh warping methods used to develop our combined level set/mesh warping approach in this paper. These methods are the energy minimization formulation of the level set method due to Chan and Vese and the finite element-based mesh warping (FEMWARP) method due to Shontz and Vavasis.

3.1 Level Set Methods

In this section, we give an introduction to the level set method and describe the particular level set method used in our work. The level set method is a numerical technique for tracking evolving interfaces, shapes, curves, or surfaces. The level set method was developed by Osher and Sethian in 1987 initially for problems in fluid dynamics [55]. However, there has been a significant amount of research on level set methods by numerous researchers, which has allowed for numerous extensions of the method and its applications to numerous other fields. Two significant advantages of level set methods are: (1) the deforming curve or shape need not be parametrized and (2) deforming shapes undergoing topological changes can easily be tracked. These advantages make the level set method ideal for tracking the evolution of the ventricles of the hydrocephalic brain.

3.1.1 The Chan and Vese Level Set Method for Curve Evolution

Here we describe the basic level set method for curve evolution [55]. First we define some notation. Let Ω prescribe a bounded open subset of \mathbb{R}^2 , with boundary given by $\delta\Omega$. Let $u_0 : \bar{\Omega} \rightarrow \mathbb{R}$ denote a given image and $C(s) : [0, 1] \rightarrow \mathbb{R}^2$ denote a parametrized curve. In level set methods, implicit representation of the curve C is given by a Lipschitz function ϕ . That is, $C = \{(x, y) | \phi(x, y) = 0\}$. The zero-level curve of the function at time t of the function $\phi(t, x, y)$ is used to evolve C . In order to evolve the curve C , a speed and direction must be prescribed.

The level set method we use in this paper is due to Chan and Vese and evolves the level set curve based on a level set formulation of an energy functional minimization [10]. In particular, suppose that $C \subset \Omega$ is given by the zero level set of a Lipschitz function $\phi : \Omega \rightarrow \mathbb{R}$ satisfying the following properties:

$$\begin{aligned} C &= \partial\omega = \{(x, y) \in \Omega : \phi(x, y) = 0\} \\ \text{inside}(C) &= \omega = \{(x, y) \in \Omega : \phi(x, y) > 0\} \\ \text{outside}(C) &= \Omega \setminus \bar{\omega} = \{(x, y) \in \Omega : \phi(x, y) < 0\}, \end{aligned} \tag{1}$$

where C is the boundary of ω .

Let c_1 and c_2 denote constants depending on C which denote the averages of u_0 inside and outside of C , respectively, and let $F(c_1, c_2, \phi)$ denote the energy functional to be minimized. Furthermore, denote by $\mu \geq 0, \nu \geq 0, \lambda_1$, and λ_2 fixed parameters and by H_ϵ and δ_ϵ regularized Heaviside functions and one-dimensional Dirac measures.

Then the regularized energy functional which is minimized to obtain the curve evolution is defined as follows:

$$\begin{aligned}
F_\varepsilon(c_1, c_2, \phi) = & \mu \int_\Omega \delta_\varepsilon(\phi(x, y)) |\nabla \phi(x, y)| \, dx \, dy \\
& + \nu \int_\Omega H_\varepsilon(\phi(x, y)) \, dx \, dy \\
& + \lambda_1 \int_\Omega |u_0(x, y) - c_1|^2 H_\varepsilon(\phi(x, y)) \, dx \, dy \\
& + \lambda_2 \int_\Omega |u_0(x, y) - c_2|^2 (1 - H_\varepsilon(\phi(x, y))) \, dx \, dy.
\end{aligned} \tag{2}$$

Letting $\phi(0, x, y) = \phi_0(x, y)$ denote the initial contour, then the speed of the level set is given by

$$\begin{aligned}
\frac{\partial \phi}{\partial t} = & \delta_\varepsilon(\phi) \left[\mu \operatorname{div} \left(\frac{\nabla \phi}{|\nabla \phi|} \right) - \nu - \lambda_1 (u_0 - c_1)^2 + \lambda_2 (u_0 - c_2)^2 \right] = 0 \text{ in } (0, \infty) \times \Omega, \\
\phi(0, x, y) = & \phi_0(x, y) \text{ in } \Omega, \\
\frac{\delta_\varepsilon(\phi)}{|\nabla \phi|} \frac{\partial \phi}{\partial \mathbf{n}} = & 0 \text{ on } \partial \Omega,
\end{aligned} \tag{3}$$

where \mathbf{n} denotes the exterior normal boundary $\partial \Omega$, and $\partial \phi / \partial \mathbf{n}$ denotes the normal derivative of ϕ at the boundary. More details are given in [10].

We solve the energy minimization formulation of the level set method for the curve evolution given by (2) and (3) using the Matlab implementation by Wu in [92].

3.2 Mesh Warping Methods

In this section, we describe mesh warping techniques for biomedical applications and the three-step finite element-based mesh warping (FEMWARP) method (see, e.g., [4]). Mesh warping methods are numerical techniques for deforming a mesh from a source to a target domain. Such techniques are needed when the geometric domain of interest deforms of a function of time, and the mesh must be updated at each time step in response to the deforming domain boundary in order for the mesh to remain a valid approximation of the geometry.

3.2.1 The Shontz and Vavasis Finite Element-Based Mesh Warping (FEMWARP) Algorithm

We base our description of the FEMWARP method upon the presentation of the algorithm given in [74]. Let M denote a triangular finite element mesh on a two-dimensional domain, Ω . Let b and m denote the numbers of boundary and interior vertices of M , respectively, and let $n = m + b$ denote the total number of vertices.

The first step of the FEMWARP algorithm is to represent each interior vertex in M as a specific linear combination of its neighboring vertices. In order to determine the weights the linear combination for each interior vertex, the $(m + b) \times (m + b)$ global stiffness matrix A for the following boundary value problem

$$\Delta u = 0 \quad \text{on } \Omega$$

with $u = u_0$ on $\partial\Omega$ is formed, where A is computed based on piecewise linear finite elements on M . Because only the relevant matrix is kept, any u_0 may be prescribed. (For a mathematical description of the entries in A , see [31].)

For simplicity, assume that the interior vertices of M are labeled $1, 2, \dots, m$ and that the boundary vertices are labeled $m+1, m+2, \dots, n$. Next, partition A as

$$A = \begin{pmatrix} A_I & A_B \\ A_B^T & X \end{pmatrix},$$

where A_I is $m \times m$, A_B is $m \times b$, and X is $b \times b$.

Next, let x be a vector containing the x -coordinates of the initial mesh vertices. Because any linear function of the coordinates lies in the null-space of the discretized Laplacian operator, it follows that $[A_I, A_B]x = 0$. A similar identity holds for the y -coordinates. Equivalently,

$$A_I x_I = -A_B x_B. \quad (4)$$

To represent each interior vertex as a linear combination of its neighboring vertices, one can divide each row of $[A_I, A_B]$ by the diagonal element in that row. This yields a linear system whose diagonal entries are 1's and whose row sums are 0's. Hence, each interior vertex is represented as a linear combination of its neighboring vertices.

The second step of the FEMWARP method is to transform the boundary vertices to new positions by applying a user-prescribed boundary deformation. Denote the new boundary vertex positions by $[x_B, y_B] \rightarrow [\hat{x}_B, \hat{y}_B]$.

The third step of the FEMWARP algorithm is to solve the above linear system of equations, i.e., (4) with a new right-hand side vector based on the new positions of the boundary vertices for the new coordinates of the interior vertices of \hat{M} on $\hat{\Omega}$. In particular, we solve (5)

$$A_I [\hat{x}_I, \hat{y}_I] = -A_B [\hat{x}_B, \hat{y}_B] \quad (5)$$

for $[\hat{x}_I, \hat{y}_I]$.

FEMWARP maintains the topology of the mesh when warping M to \hat{M} ; hence the mesh is fully satisfied after solving (5).

4 Ventricular Deformation for Boundaries Obtained from the Level Set Method and FEMWARP in Hydrocephalic Patients

Assuming as input medical images of the brain of a hydrocephalic patient taken at different times, a combined level set/ mesh warping approach can be designed in order to track the evolution of the brain ventricles. In particular, the level set method given by (2) and (3) can be used in order to segment the medical images and determine the ventricular boundaries. The FEMWARP mesh warping technique described in Section 3.2 can be used to deform the ventricular geometry from the source

to the target ventricular boundary. Our combined approach is used in a computational pipeline involving the following steps: image denoising, image segmentation, obtaining boundary vertices via the level set method, mesh generation, mesh warping, and mesh quality improvement. Pseudocode for our proposed computational pipeline is shown in Algorithm 1. The following subsections give more details about each step in our computational pipeline.

Algorithm 1 Mesh warping with the level set method

```

1: Input:  $X \leftarrow$  medical image having initial ventricular boundary
2:        $Y \leftarrow$  medical image having goal ventricular boundary
3: Image denoising using mask filters
4: Image segmentation via thresholding method
5:
6: Obtain ventricular boundary vertices from segmented  $X$  and  $Y$  medical images
   via level set method
7:  $A \leftarrow$  ventricular boundary vertices for  $X$ 
8:  $B \leftarrow$  ventricular boundary vertices for  $Y$ 
9:
10: Generate initial mesh with  $A$  using Triangle
11:
12: LOOP 1: Deform mesh from  $A$  to  $B$  using FEMWARP
13: if mesh is valid then
14:   Mesh quality improvement on the deformed mesh
15:   return mesh
16: else
17:    $n = 1$  // Intermediate mesh deformation
18:   while mesh is invalid do
19:      $C \leftarrow (\frac{1}{2})^n (B - A)$ 
20:     Deform mesh from  $A$  to  $C$  using small-step FEMWARP
21:      $n = n + 1$ 
22:   end while
23:   Mesh quality improvement on the deformed mesh
24:    $A \leftarrow C$ 
25: end if
26:
27: Go to LOOP 1

```

4.1 Image Denoising

In order to obtain the boundary vertices of the ventricles in the medical images, image denoising is first performed. By applying the appropriate mask filter to the image, the image is denoised and the image becomes easy to recognize the object.

4.2 Image Segmentation

After image denoising is performed, the image is segmented by a thresholding method. The method selects an appropriate threshold value for the image and divides the image into two parts: the ventricles and outside the ventricles based on the threshold value. In the segmented image, the white-colored parts represent the ventricles we want to deform.

4.3 Obtaining Boundary Vertices

The level set method is then employed in order to obtain the boundary vertices of the ventricles in the post-treatment image. The contour constructed by the boundary vertices for the ventricles in the segmented pre-treatment image is used as the zero level set which is the input of the level set method.

Given the zero level set, the level set method moves the contour along its interior normal, and the contour evolves until it matches the boundary of the ventricles in the segmented post-treatment image.

4.4 Mesh Generation

The mesh used as an input for mesh warping is generated based on the boundary vertices of the ventricles in the segmented pre-treatment image. To generate the initial mesh, Triangle [71] is employed.

4.5 Mesh Deformation

To track the movement of the ventricles in the brain when hydrocephalus is treated by shunt insertion, the initial mesh is deformed until it matches the target ventricular boundary vertices for post-treatment. To deform the mesh, the FEMWARP [74] algorithm (see Section 3.2 for a description) is used.

When mesh deformation is performed, the deformed mesh may become tangled due to a large deformation. In this case, intermediate deformation steps are generated based on performing a backtracking line search between the pre- and post-treatment ventricular boundary vertices. Thus, a target which will yield a valid deformed mesh can be designed. An invalid mesh element can be detected by computing the sign of the determinant of an element's Jacobian matrix and comparing it to its original sign. If a tangled mesh is generated by the deformation, a backtracking line search brings the deformed vertices back to the halfway point of the deformation between the source and target vertex locations. This reduces the deformation size and prevents tangling. Small-step FEMWARP can then be used to successfully deform the mesh.

4.6 Mesh Quality Improvement

The deformed meshes often have poor mesh quality since large deformations cause poorly-shaped elements near to the moving ventricular boundary. It is well-known that the mesh quality effects the time to solve PDE, the condition number of the numerical linear system, and the accuracy of the PDE solution [72].

Hence, in order to improve the quality of the deformed meshes, mesh quality improvement is performed using the Mesh Quality Improvement Toolkit (Mesquite) Version 2.1.4 [8]. The objective function used in this study is

$$f(x) = \frac{1}{n} \sum_{1 \leq i \leq n} q_i^2, \quad (6)$$

where f is the overall mesh quality as measured by the average of the sequence of the element qualities, q_i is the quality of element i , and n is the number of elements in the mesh.

The inverse mean ratio metric [50] was used as the mesh quality metric for the mesh optimization in (6). The formula for computing the inverse mean ratio of an element is given by

$$q = \frac{\|AW^{-1}\|_F^2}{2 \det(AW^{-1})}, \quad (7)$$

where A is the Jacobian matrix for the physical triangle, and W is a Jacobian matrix for the reference triangle. The range for this quality metric is 1 to ∞ for non-inverted elements. Inverted elements correspond to a negative value of the metric. Since an equilateral triangle is the ideal element for the mesh optimization procedure in this study, 1 is the ideal value of the metric. Hence, lower values of the metric correspond to meshes with better quality.

During the mesh optimization process, the boundary vertices are held fixed. In addition, the initial meshes and subsequent meshes are not allowed to contain any inverted elements. In order to minimize (6), a local implementation of the feasible Newton method [50] is employed. We terminate the mesh optimization process af-

ter obtaining the same value of the objective function to six digits of accuracy on successive iterations.

5 Simulations of the Evolution of the Brain Ventricles in Hydrocephalic Patients

Three simulations were designed to track the evolution of the brain ventricles upon treatment of hydrocephalus via shunt insertion. The simulations were performed based on our proposed combined level set/mesh warping algorithm (see Algorithm 1). The level of difficulty varied in these simulations, from simple to complex based on the specific deformation of the ventricles. Two medical image sets derived from [89] were used in simulations. The first set of medical images included two CT images, corresponding to pre- and post-treatment. The second set included three CT images, corresponding to pre-treatment and two time periods post-treatment. The Solaris machine used for the simulations of the evolutions of the ventricles was an UltraSPARC-III CPU with a 750MHz processor, 1GB SDRAM of memory, and an 8MB L2 cache.

5.1 Simulation 1: Small Decrease in the Area of the Ventricles

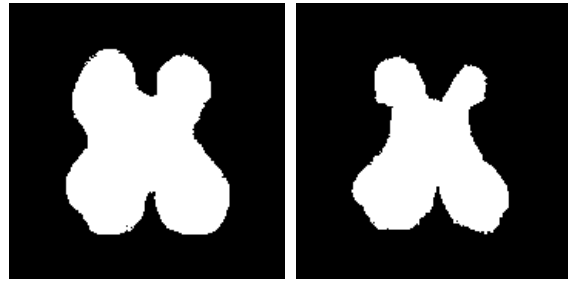
We obtained pre- and post-treatment (three months later) CT images [89] for a hydrocephalic patient who was treated by shunt insertion. In this simulation, the sixth line in Algorithm 1 was performed manually without using the level set method. Since we tested a simple case of the deformation in this simulation, the lines from 16 to 25 in Algorithm 1 (intermediate mesh deformation) were not performed. To track the evolution of the brain ventricles, the images were first denoised by using a 4×4 mask filter for both images.

After denoising the images, the images were segmented based on a threshold value for the pixels. For this simulation, a threshold value of 20 was applied. The images obtained from image denoising and image segmentation are shown in Fig. 1. In the segmented images, the white-colored parts represent the ventricles containing CSF whose evolution was tracked in our numerical simulation.

Once image segmentation was performed, the boundary vertices were easily obtained. By tracing the shape of the ventricles, the boundary vertices used in the mesh generation step were obtained. Fig. 2 shows the boundary vertices obtained from the segmented images. Each ventricular boundary contains 225 vertices in the boundary. Each vertex has the same Euclidean distance from itself to its neighboring vertices.

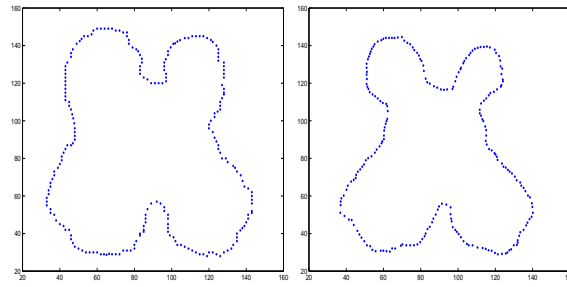
After the boundary vertices were obtained from the segmented images, the initial mesh for the boundary vertices of pre-treatment image was generated using Triangle [71]. The mesh contained 2298 vertices and 4245 elements, and its initial quality is given in Table 1. Based on the initial mesh and the final ventricular boundary ver-

Fig. 1 Two segmented images: pre- and post-treatment. The image was denoised with a 4×4 mask filter. After image denoising, the images were segmented.



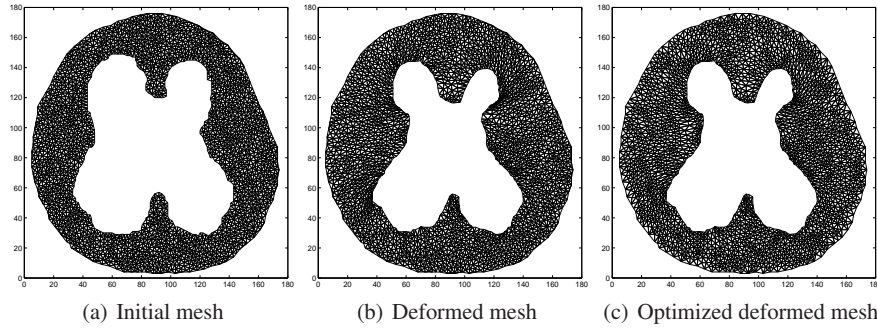
(a) Segmented pre-treatment image (b) Segmented post-treatment image

Fig. 2 Boundary vertices obtained from pre- and post-treatment segmented images. The ventricular boundary movement due to shunt insertion were shown.



(a) pre-treatment (b) post-treatment

tices obtained from the post-treatment image, mesh deformation for tracking the shape evolution of the brain ventricles was performed via FEMWARP [74].



(a) Initial mesh (b) Deformed mesh (c) Optimized deformed mesh

Fig. 3 (a) Initial mesh generated by Triangle [71] and (b) the deformed mesh generated by FEMWARP mesh warping algorithm. (c) Mesh quality improvement was performed on the deformed mesh to improve the mesh quality.

The initial mesh and the deformed meshes resulting from mesh deformation and mesh quality improvement procedures are shown in Fig. 3. Since the area of the

ventricles was decreased as keeping similar shapes in this simulation, the deformation was small. Because of this, FEMWARP easily controlled the deformation, so a tangled mesh was not generated.

As the final step of the simulation, the deformed mesh was optimized to improve the mesh quality by using Mesquite [8]. Table 1 and Fig. 4 show the mesh quality statistics and the quality distribution for each mesh generated during the simulation.

Table 1 Inverse mean ratio mesh quality statistics for several meshes used in the simulation. The feasible Newton method [50] implemented in Mesquite [8] was used for average mesh quality improvement.

Mesh	Inverse mean ratio mesh quality				
	min	avg	rms	max	std
Initial mesh	1.00002	1.05555	1.05816	2.0110	0.07427
Deformed mesh	1.00001	1.31565	2.36839	82.6890	1.96934
Optimized mesh	1.00000	1.14067	1.15345	3.8571	0.18090

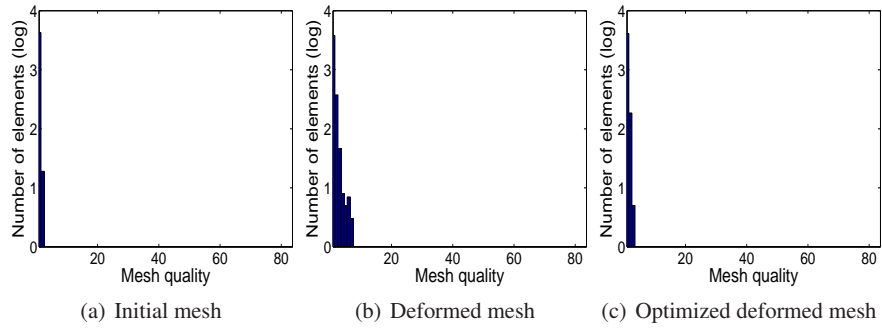
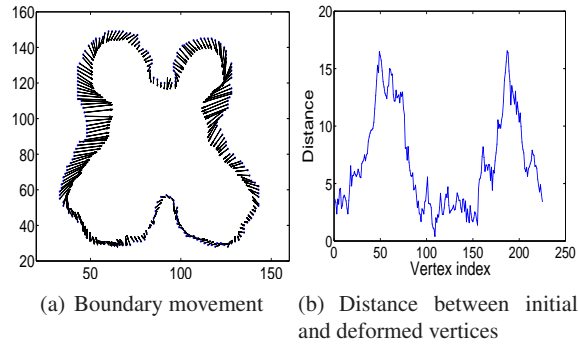


Fig. 4 Inverse mean ratio mesh quality distribution for meshes generated in Simulation 1.

The average mesh quality of the initial mesh was 1.05555. After mesh deformation, the mesh quality of the deformed mesh was 1.31565. The number of good quality elements decreased from 1550 to 1050. By performing mesh quality improvement, the quality of the deformed mesh was improved to 1.14067. The number of poor quality elements decreased by more than half compared to the unoptimized deformed mesh. The number of high quality elements (i.e., those with quality values ranging from 1 to 1.2) increased from 1700 to 2400 due to the mesh optimization process. Also, the quality of the worst element in the deformed mesh improved significantly from 82.689 to 3.857.

The distances for each boundary vertex during the deformation are visualized in Fig. 5. The distances were computed by calculating the Euclidean distance be-

Fig. 5 Boundary movement of each vertex and their corresponding distances between pre- and post-treatment deformation.



tween corresponding ventricular boundary vertices in the pre- and post-treatment images. During the mesh deformation, the shapes of the ventricles containing the CSF changed. Since the sizes of the vectors in the middle-left and the upper-right parts of the ventricles were bigger than the corresponding vectors for the other parts, more boundary vertex movement occurred in the middle-left and the upper-right parts of the ventricles compared to the other parts. It is also shown in Fig. 5(b) that the boundary vertex movements around the vertices indexed 50 and 200 were larger than those of other vertices. Note that the boundary vertices were indexed from the starting point (90,59) and moving in a clockwise direction.

5.2 Simulation 2: Asymmetric Ventricular Shape Change

Three CT images [89] were used in the simulation: pre-treatment, period 1 (six months later), and period 2 (one year later). The goal of this experiment was to simulate ventricular deformation from pre-treatment to period 1 and from period 1 to period 2. In this simulation, the intermediate mesh deformation in Algorithm 1 (i.e., lines 16 through 25) was performed. Also, similar to the previous simulation, the ventricular boundary vertices were obtained with a manual process, and not with the level set method specified in the sixth line in Algorithm 1.

To reduce the noise in the image, a 3×3 mask filter for the pre-treatment CT image, a 6×6 mask filter for the period 1 CT image, and a 4×4 mask filter for the period 2 CT image were applied. After image denoising was performed, the images were segmented based on an appropriate threshold value. In this simulation, the threshold values 20, 77, 45 were used for the pre-treatment, period 1, and period 2 images. The segmented images to be used for obtaining the boundary vertices are shown in Fig. 6. The white-colored parts in the segmented images represent the brain ventricles which deform as their fluid volumes decrease after the treatment via shunt insertion.

The boundary vertices obtained from the segmented images are shown in Fig. 7. For each boundary vertex, the next vertex is selected from the boundary vertices

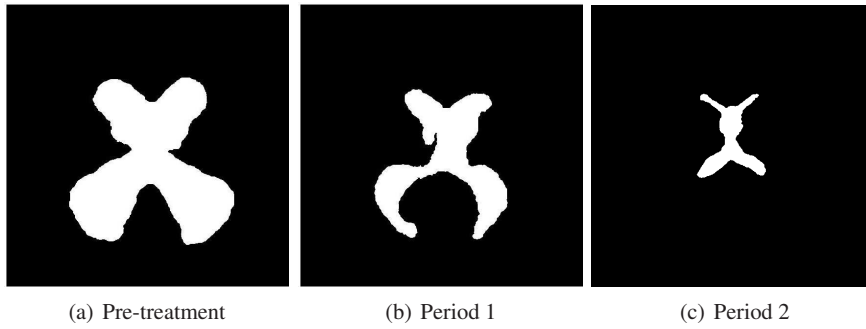


Fig. 6 Segmented images for obtaining the boundary vertices from the given three CT images: (a) pre-treatment, (b) period 1 (six months later), and (c) period 2 (one year later). The white-colored parts represent the ventricles which deform as their fluid volume decrease after shunt insertion.

with a fixed Euclidean distance from the given vertex. The boundary vertices were computed and ordered by repeating this process.

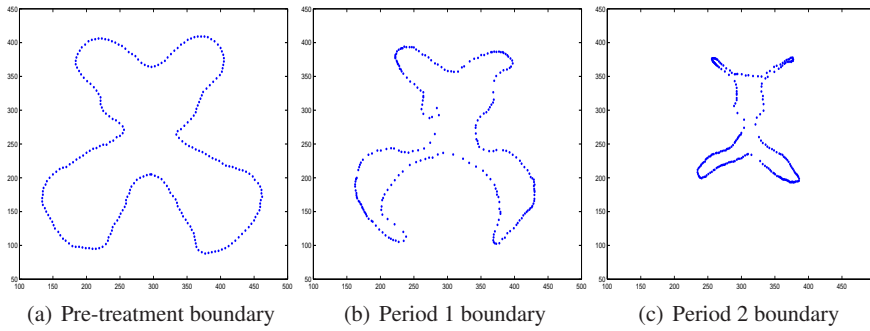
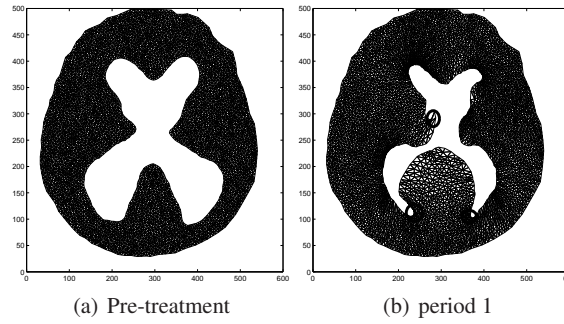


Fig. 7 Boundary vertices obtained from the segmented images: pre-treatment, period 1, and period 2.

Using the ventricular boundary vertices for pre-treatment, the initial mesh was generated using Triangle [71]. The mesh contained 4311 vertices and 8166 elements; its mesh quality is given in Table 2. By using the boundary vertices obtained from the segmented images, the first mesh deformation step from pre-treatment to the period 1 boundary was performed via FEMWARP [74]. Mesh deformation results from the initial mesh to the period 1 boundary are shown in Fig. 8.

As can be seen in Fig. 8, since inverted elements were generated during mesh warping, the deformed mesh cannot be used as an input mesh for the next deformation step, as tangled meshes are not allowed to be used as an input for finite element methods, including methods such as FEMWARP which are based on a finite element method. The majority of the inverted elements were located in the marked area

Fig. 8 The first mesh deformation of the ventricular boundary from pre-treatment to period 1. Inverted elements exist in the marked areas where a large deformation occurred.



shown in Fig. 8(b). Compared to the other ventricular boundary areas, the mesh deformation in the marked areas was larger. To avoid tangled mesh generation, several intermediate mesh deformation steps for use with small-step FEMWARP [73] were designed. The intermediate steps showed more details of the ventricular evolution when the hydrocephalus was treated by shunt insertion.

To generate the intermediate mesh deformation steps, the new boundary vertices between the pre-treatment and period 1 boundary vertices were obtained by manual selection of the intermediate boundary vertices. By using the newly obtained boundary vertices, the mesh deformation was performed. Since adding the intermediate mesh deformation steps decreased the size of the deformation, small-step FEMWARP easily handled the deformation without generating inverted elements in the deformed meshes.

Nine total intermediate mesh deformation steps were designed from the initial mesh generated by pre-treatment boundary vertices to the deformed mesh to be generated by period 1 boundary vertices. Fig. 9 shows the mesh deformation results from pre-treatment to the period 1 ventricular boundaries with intermediate deformation steps. In Fig. 9, the initial mesh, the meshes resulting from the sixth deformation, and the meshes resulting from the ninth deformation are shown.

Mesh quality improvement was performed for each deformed mesh before deforming the mesh again in order to improve the mesh quality. The inverse mean ratio mesh quality statistics and element quality distribution results are shown in Table 2 and Fig. 10.

The average quality of the initial mesh was 1.11483 according to the inverse mean ratio mesh quality metric. The average quality of the sixth intermediate mesh improved from 1.13918 to 1.1326 by performing mesh quality improvement. The worst mesh quality of an element in the sixth intermediate mesh showed a noticeable improvement as a result of mesh quality improvement, as it decreased from 10.9184 to 5.1703.

The ventricular boundary vertices in the ninth intermediate mesh matched exactly the ventricular boundary vertices obtained from the segmented image for period 1. Due to mesh quality improvement, the average mesh quality improved from 1.16464 to 1.15143; the worst mesh quality of an element in the ninth intermediate mesh improved from 14.5821 to 6.57973.

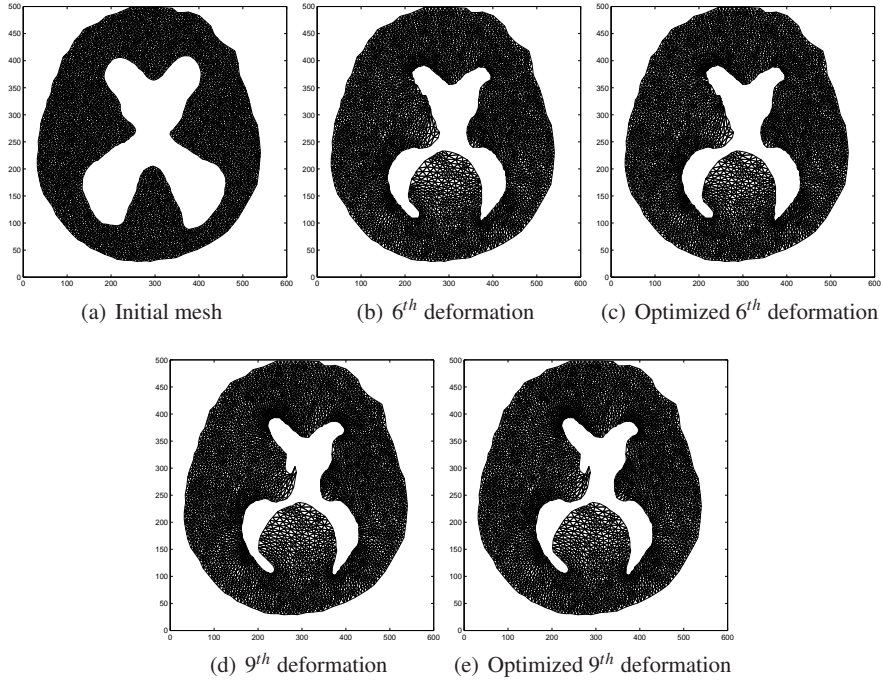


Fig. 9 (a) The initial mesh generated by using Triangle [71] and (b) and (d) the deformed meshes generated by the FEMWARP algorithm [74]. The mesh resulting from the ninth deformation matched to the boundary vertices of the ventricles for period 1. (c) and (e) The improved deformed meshes after use of mesh quality improvement.

Table 2 Inverse mean ratio mesh quality statistics for several meshes used in the simulation of the ventricular mesh deformation from pre-treatment to period 1. The feasible Newton method [50] implemented in Mesquite [8] was used for average mesh quality improvement.

Mesh	Inverse mean ratio mesh quality				
	min	avg	rms	max	std
Initial mesh	1.00000	1.11483	1.12096	2.4723	0.11708
6^{th} deformation	1.00000	1.13918	1.17003	10.9184	0.26693
Opt. 6^{th} deformation	1.00002	1.13266	1.16431	5.1703	0.26964
9^{th} deformation	1.00001	1.16464	1.19760	14.5821	0.27905
Opt. 9^{th} deformation	1.00001	1.15143	1.19106	6.5797	0.30469

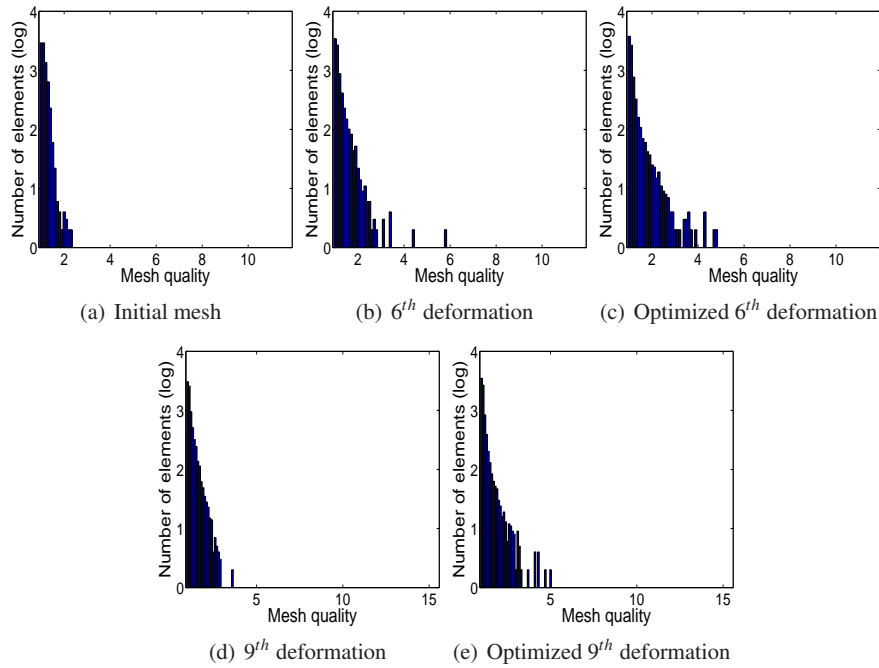


Fig. 10 Inverse mean ratio element quality distribution for the meshes generated in Simulation 2 (ventricular mesh deformation from pre-treatment to period 1). Quality distributions for (a) the initial mesh, (b) the sixth intermediate mesh, (c) the sixth intermediate mesh after mesh quality improvement was performed, (d) the ninth intermediate mesh, and (e) the ninth intermediate mesh after mesh quality improvement was performed.

In Fig. 10, it can be seen that most of the mesh elements (approximately 90% of the elements) for the ninth intermediate mesh had good mesh qualities after mesh quality improvement was performed. Also, the number of poor quality mesh elements decreased. Since the poor quality mesh elements tended to generate inverted elements if the mesh was used as an input for the mesh deformation, reducing the number of poor quality mesh elements makes the next intermediate mesh deformation step more likely to succeed.

From the ninth intermediate mesh, the deformation to the ventricular boundary for period 2 was performed. After six of the intermediate meshes were generated, the boundary vertices of the deformed mesh matched to the boundary vertices of the ventricles in the segmented period 2 image. Fig. 11 shows the mesh deformation results from period 1 to period 2. Six intermediate deformation steps were generated for this part of the simulation. In this figure, the mesh which having the boundary vertices matched to the ventricular boundary vertices for period 1, the twelfth intermediate step, and the fifteenth intermediate step are shown. The ventricular boundary vertices in the fifteenth intermediate mesh matched exactly the ventricular boundary vertices for period 2.

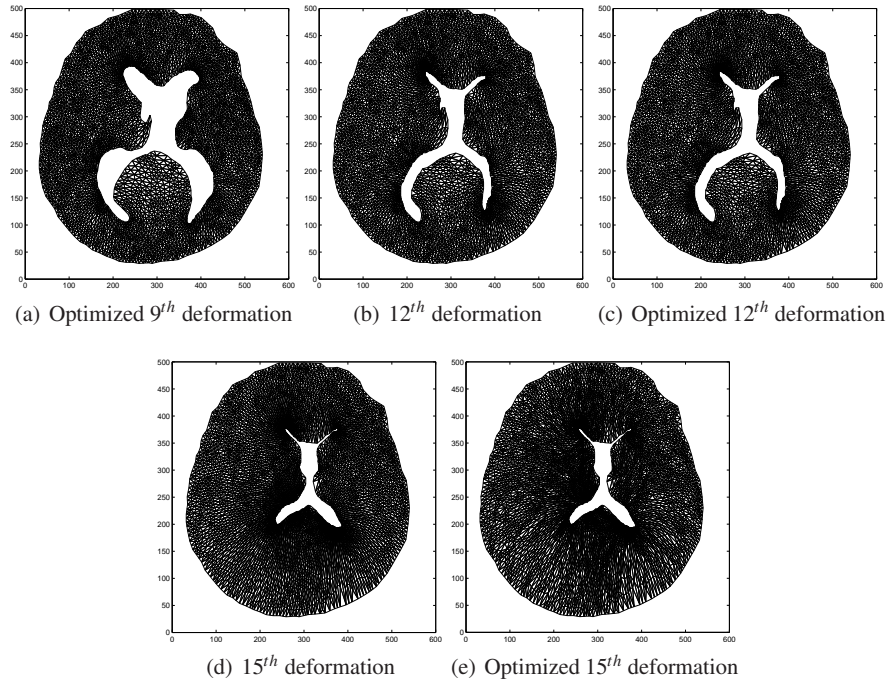


Fig. 11 (a) the mesh having the ventricular boundary vertices matched to period 1 ventricular boundary vertice. (b) and (d) the deformed meshes generated by the FEMWARP algorithm [74]. The fifteenth intermediate mesh deformation result matched exactly to the boundary vertices for the ventricles in the segmented period 2 image. (c) and (e) mesh quality improvement was performed to improve the quality of the meshes at each step of the hydrocephalus ventricular deformation.

Mesh deformation from period 1 to period 2 boundary of the ventricles was easier than that for pre-treatment to period 1. Mesh deformation from period 1 to the period 2 ventricular boundary required fewer intermediate mesh deformation steps than did the earlier part of the simulation. This is because the ventricles shrunk significantly, allowing for more feasible possibilities for interior vertex positions.

Table 3 and Fig. 12 show the inverse mean ratio mesh quality improvement results and the quality distribution for the deformed meshes from the simulation of the ventricular deformation from period 1 to period 2.

As shown in Table 3, the average mesh quality for the twelfth intermediate mesh improved from 1.2625 to 1.24535. The worst mesh quality also improved from 20.1674 to 11.8054. Fig. 12 shows that approximately 90% of the mesh elements in the twelve intermediate mesh have good mesh qualities after mesh quality improvement was performed.

Although the average mesh quality of the fifteenth intermediate mesh improved from 1.57492 to 1.53606 by performing mesh quality improvement with Mesquite [8], still many poor mesh quality elements existed in the mesh, and the worst mesh qual-

Table 3 Inverse mean ratio mesh quality statistics for several meshes used in the simulation. The feasible Newton method [50] implemented in Mesquite [8] was used for average mesh quality improvement. For improving the worst quality of the final mesh, the PS mesh quality improvement algorithm [57] was applied to obtain further improvement.

Mesh	Inverse mean ratio mesh quality				
	min	avg	rms	max	std
12 th deformation	1.00001	1.26625	1.36000	20.1674	0.49619
Opt. 12 th deformation	1.00001	1.24535	1.34960	11.8054	0.52010
15 th deformation	1.00020	1.57492	1.70020	6.7762	0.64054
Opt. 15 th deformation	1.00002	1.53606	1.81146	18.4508	0.96015
Opt. 15 th deformation (with PS)	1.00015	1.68952	1.78281	4.3440	0.56913

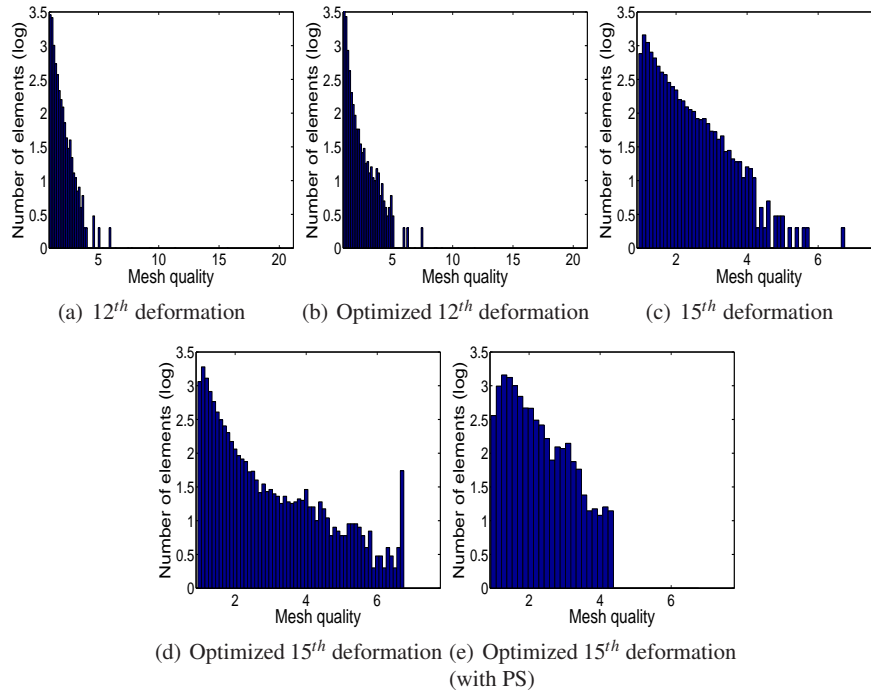


Fig. 12 Inverse mean ratio mesh quality distribution for meshes generated in Simulation 2 (ventricular mesh deformation from period 1 to period 2). Quality distribution for (a) the twelfth intermediate mesh, (b) the twelfth intermediate mesh after mesh quality improvement was performed, (c) the fifteenth intermediate mesh, (d) the fifteenth intermediate mesh after mesh quality improvement was performed, and (e) the fifteenth intermediate mesh after the worst quality element improvement was performed.

ity of the fifteenth intermediate mesh degraded from 6.7762 to 18.4508. Thus, to reduce the number of poor quality mesh elements, mesh quality improvement of the worst mesh element was performed by using the pattern search (PS) mesh quality improvement algorithm [57]. By using this algorithm, the quality of the worst mesh element improved from 18.4508 to 4.3440. Most of the mesh elements had good mesh qualities, in spite of the fact that the average quality of the mesh increased slightly to 1.68952.

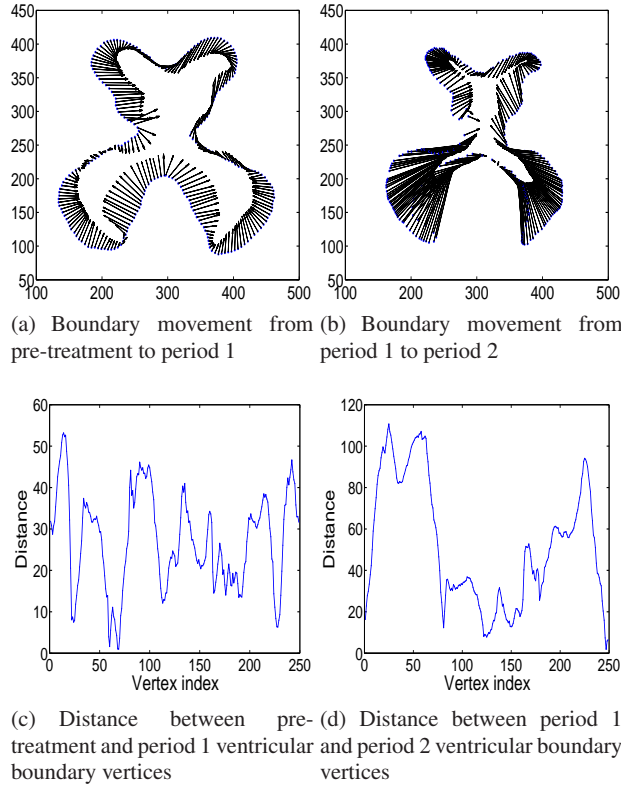


Fig. 13 (a) boundary movement of each vertex from pre-treatment to period 1, (b) boundary movement of each vertex from period 1 to period 2, (c) the distance between the pre-treatment and period 1 vertices, (d) the distance between the period 1 and period 2 vertices.

The distances for boundary vertex movement during the deformations are visualized in Fig. 13. For the deformation from pre-treatment to period 1, most of the ventricular boundary vertices moved symmetrically except in the middle-left parts of the ventricles. The shapes for the middle-left parts of the ventricles changed significantly more than that of middle-right parts. This is because the shunt was inserted in the ventricles in this spot in order to treat the hydrocephalus. The sizes of the vectors in the two lower parts and upper-left parts of the ventricles were bigger than the

sizes of the corresponding vectors for the other parts. Fig. 13(c) shows the distances from the pre-treatment to the period 1 ventricular boundary vertices. The distances are computed by calculating the Euclidean distance from pre-treatment ventricular boundary vertices the corresponding vertices in period 1. Note that they do not represent the cumulative distances moved during the mesh warping procedure. As can be seen in Fig. 13(c), the boundary vertex movements around the vertices indexed 5, 100, and 240 were larger than those of the other vertices.

In the case of the deformation from period 1 to period 2, most of the ventricular boundary vertices showed large movements during the deformation. In Fig. 13(b), the changing shapes of the lower parts of the ventricles were especially noticeable. As can be seen in Fig. 13(d), although the boundary vertex movements for most of the vertices were large, the boundary vertices located in the lower parts of the ventricles (indexed between 0 and 70 and between 230 and 250) showed the largest movement in the deformation from period 1 to period 2.

During the treatment of hydrocephalus, the brain size also changed. In particular, the brain size increased due to infant growth. The brain boundaries obtained from the segmented images are shown in Fig. 14.

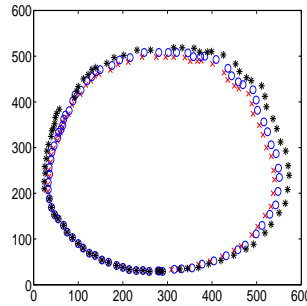


Fig. 14 Brain boundary vertices obtained from the segmented images. The \times , o , and $*$ symbols represent the pre-treatment, period 1, and period 2 brain boundaries, respectively.

Mesh deformation results from pre-treatment to period 1 and from period 1 to period 2 are shown in Fig. 15. In each step, deformation of both the ventricles and the brain were performed.

5.3 Simulation 3: Ventricular Deformation with Boundaries Obtained via the Level Set Method

In simulation 2, the ventricular boundary vertices in the segmented images were manually determined. Furthermore, the intermediate steps for avoiding the generation of inverted elements in the meshes used for the simulation of the ventricular deformations were computed by manually selecting the vertices between the pre-

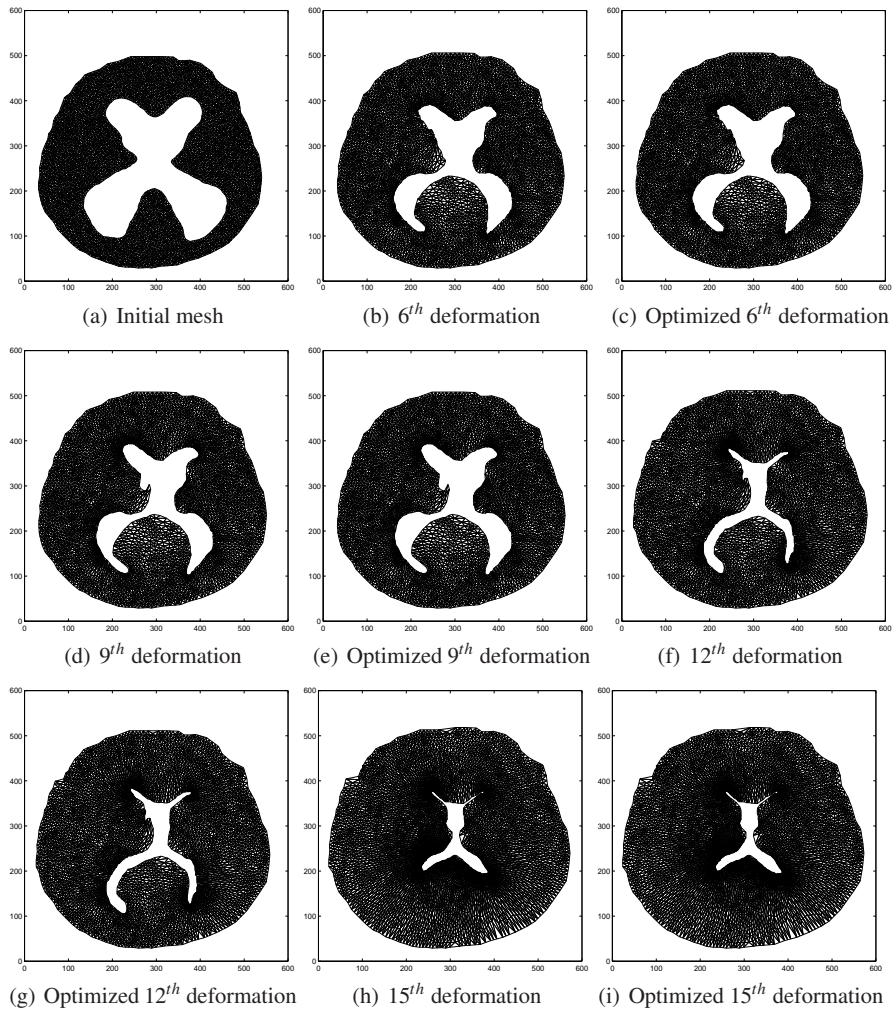


Fig. 15 (a) initial mesh generated by Triangle [71] and (b),(d),(f), and (h) the deformed meshes generated by the FEMWARP algorithm [74]. The fifteenth intermediate mesh deformation result matched exactly to the boundary vertices of the ventricles and the brain in segmented period 2 image. (c),(e),(g), and (i) mesh quality improvement was performed to improve the quality of the meshes at each step of ventricular deformation for hydrocephalus.

treatment and period 1 or between the period 1 and period 2 boundary vertices of the ventricles.

The main new aspect of this simulation is that the level set method [68] was applied to automatically obtain the boundary vertices of the ventricles in the segmented images. Using the boundary vertices, the initial mesh was generated using Triangle [71]. The mesh contained 2392 vertices and 4422 elements; its quality is given in Table 4. Also, with the boundary vertices of the ventricles in the pre-treatment, period 1, and period 2 images, the intermediate steps were automatically computed by using a backtracking line search method to obtain valid intermediate meshes.

Similar to the previous simulation, image denoising was performed as the first step of the simulation. The same mask filters were applied to denoise each medical image. After the images were denoised, image segmentation was performed based on the same threshold values used in the previous simulation. The segmented images were the same as before and are shown in Fig. 6.

The level set method was applied to obtain the boundary vertices of the ventricles in the period 1 and period 2 images. To use the level set method, the zero level set was defined and used as an input. The contour constructed by the boundary vertices for the ventricles in the segmented pre-treatment image was used as the zero level set.

To obtain the boundary vertices of the ventricles in the segmented pre-treatment image, the contours were first generated in the segmented pre-treatment image. The pixel values of the segmented images were used to generate the contours. Since the ventricles in the segmented image were represented as pixels with a value of zero and all the other parts were represented as pixels with a value of one, the contours were plotted around the ventricles in the segmented image. The contour for the zero function matched the ventricular boundary in the segmented pre-treatment image.

The contour with the zero function was used as an input of the level set method and has used to obtain the boundary of the ventricles in the segmented image for period 1. Given the zero level set, the level set method moved the contour toward its interior normal with constant speed (a value of approximately $8.854e^{-12}$ was used for ϵ_0 in this simulation). The evolution was stopped when the contour matched the ventricular boundary in the segmented period 1 image. Sixty iterations of the level set method were required to evolve the contour.

The level set method was also used to generate the boundary of the ventricles for period 1 with complicated changes of shape (where the shunt was inserted). With the ventricular boundaries obtained from the level set method, several intermediate steps were generated automatically via linear interpolation. However, it was challenging to compute the intermediate boundaries near the inserted shunt via linear interpolation. This technique generated meshes with several inverted elements; most of them were located near where the shunt was inserted. Also, determining other types of interpolation automatically would be difficult since it is hard to know what type to use. Thus, in order to avoid generation of inverted elements and to reduce the number of intermediate steps for ventricular deformation from pre-treatment to

period 1, the boundary of the ventricles for period 1 was obtained by deleting the shunt in the segmented period 1 image.

When the ventricular boundary for period 1 was obtained, the boundary was used as an input contour of the level set method which was used to obtain the ventricular boundary for period 2. Similar to the process performed for obtaining the ventricular boundary vertices for period 1, the level set method evolved the boundary of the ventricles for period 1 along its interior normal with the constant speed given above. After 53 iterations, the level set method was terminated after the new boundary matched the ventricular boundary for the segmented period 2 image.

The contours obtained by the level set method for representing the boundary of the ventricles in each segmented image included a different number of vertices. However, the same number of boundary vertices for each ventricular boundary is required for deformation using FEMWARP.

To represent the contours with the same number of vertices, an identical number of vertices were chosen from the starting positions in each segmented image. For the pre-treatment boundary, the vertex with the xy-coordinates (300,200) was used as a starting point, and every fourth vertex in the contour was selected as vertices used for representing the boundary of the ventricles for pre-treatment. From the vertex with the xy-coordinates (300, 230), every third vertex in the contour was selected to use as vertices used for the period 1 ventricular boundary. For the period 2 boundary, the vertex with the xy-coordinates (295,250) was used as a starting point for the vertex selection. Every second vertex in the contour was selected as the ventricular boundary vertices for period 2.

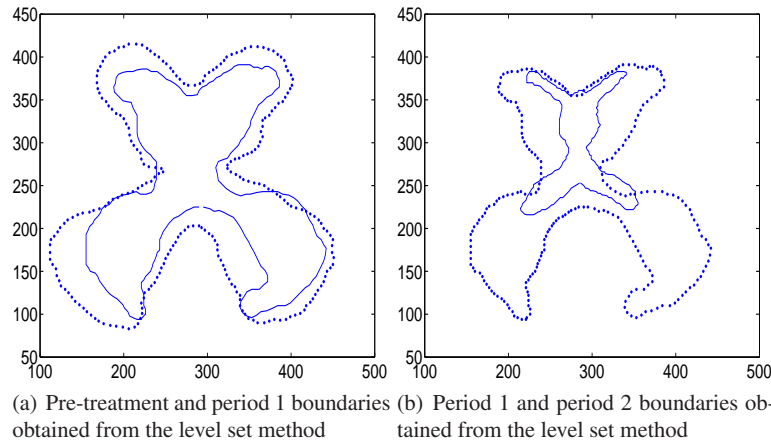


Fig. 16 Pre-treatment, period 1, and period 2 boundaries obtained from the level set method. The dotted boundaries represent the initial contour, and the solid line boundaries represent the evolved contour, which is matched to the boundary.

The boundaries of the ventricles for pre-treatment, period 1, and period 2 obtained from the level set method are shown in Fig. 16. The dotted plot in Fig. 16(a)

represents the boundary for pre-treatment generated by the contour plot with the zero function value, and the solid line plot shows the boundary for period 1 obtained by evolving the contour (dotted plot) by the level set method. In Fig. 16(b), the dotted plot is the contour which represents the boundary for period 1, and the solid line plot shows the evolved contour for the period 2 boundary obtained from the level set method.

With the boundary vertices obtained from the level set method, the evolution of the ventricles containing cerebrospinal fluid was simulated. Since the ventricular deformation both from the pre-treatment to period 1 boundaries and from the period 1 to period 2 boundaries was too large to be handled by FEMWARP [74] in just one step, intermediate small deformations were performed (i.e. using small-step FEMWARP [73]).

The intermediate steps were computed based on application of a backtracking line search method for each boundary vertex. The pseudocode for computing the intermediate steps is shown in Algorithm 1 line from 17 to 22. Mesh quality improvement for the intermediate step is performed once the deformed mesh is valid. The optimized mesh is used as an input in the computation of the next intermediate step.

Fig. 17 shows the initial mesh generated using Triangle [71] with the ventricular boundary vertices for pre-treatment and the intermediate meshes generated during ventricular mesh deformation. For each intermediate mesh, mesh quality improvement was performed.

To obtain the mesh matched to the ventricular boundary vertices for period 2, sixteen intermediate steps were performed to deform the mesh from pre-treatment to period 2. Stretched triangular elements occurred near the brain boundary in the sixteenth intermediate mesh are seen in the Fig. 17(i). This is because the significant shrinkage of the ventricles happened in the sixteenth intermediate step compared to the initial mesh. Thus, the interior vertices and correspondingly the triangular elements were strained toward the ventricular boundary for period 2 in order to cover the increased area.

The inverse mean ratio mesh quality statistics and quality distribution for the deformed meshes generated during the simulation are shown in Table 4 and Fig. 18. The average mesh quality of the initial mesh was 1.0538. When each mesh deformation was performed, the average mesh quality observed for the meshes on the intermediate steps degraded. By performing mesh quality improvement with Mesquite [8], the average mesh qualities improved from 1.20431 to 1.18070, from 1.38840 to 1.37350, and from 1.50317 to 1.47862 for the sixth, ninth, twelfth, and sixteenth intermediate meshes, respectively.

Table 4 shows that the worst mesh qualities of the intermediate meshes also improved by performing mesh quality improvement with [8]. In the case of the sixteenth intermediate mesh, the worst mesh quality was degraded from 14.021 to 19.4508, even though mesh quality improvement was performed via Mesquite [8]. To obtain further mesh quality improvement for the final mesh, mesh quality improvement of the worst quality element was performed by using the PS algorithm [57]. The worst mesh quality of the sixteenth intermediate mesh improved

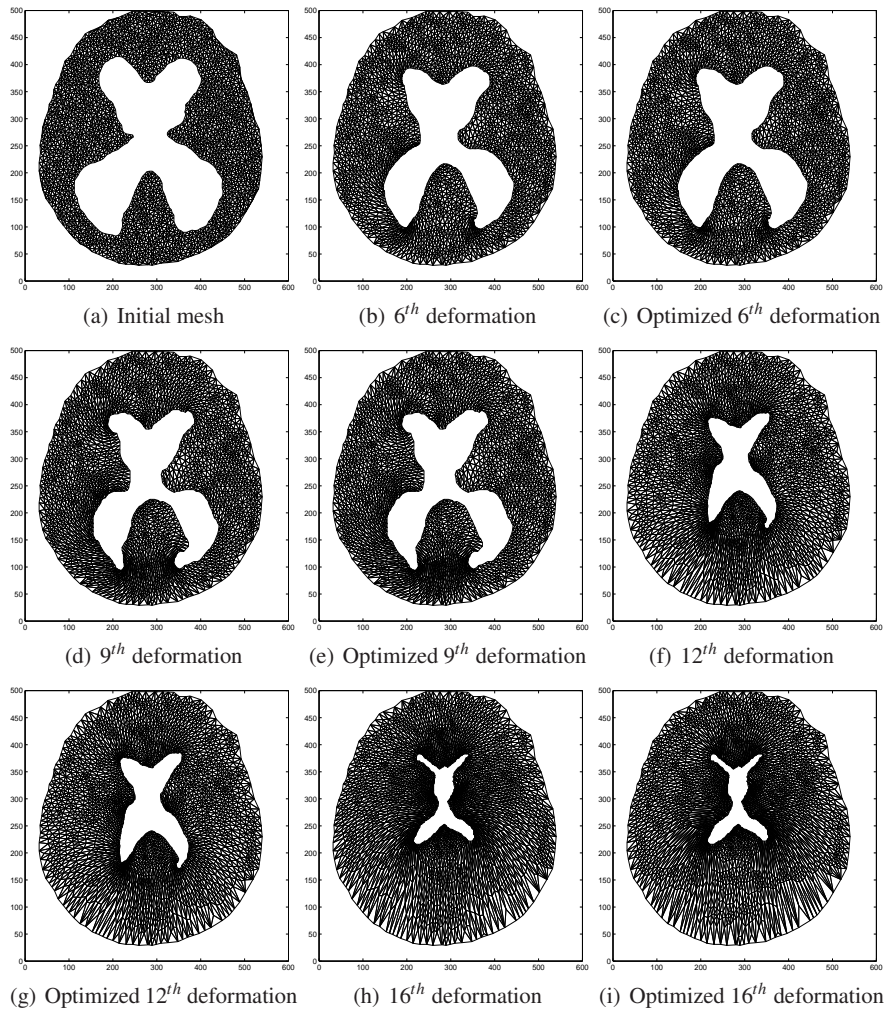


Fig. 17 (a) initial mesh generated by Triangle [71] and (b),(d),(f),and (h) the deformed meshes generated by FEMWARP [74]. The sixteenth intermediate mesh deformation result matched exactly the boundary vertices of the ventricles for period 2. (c),(e),(g), and (i) mesh quality improvement was performed to improve the quality of the meshes at each intermediate deformation step of ventricular deformation.

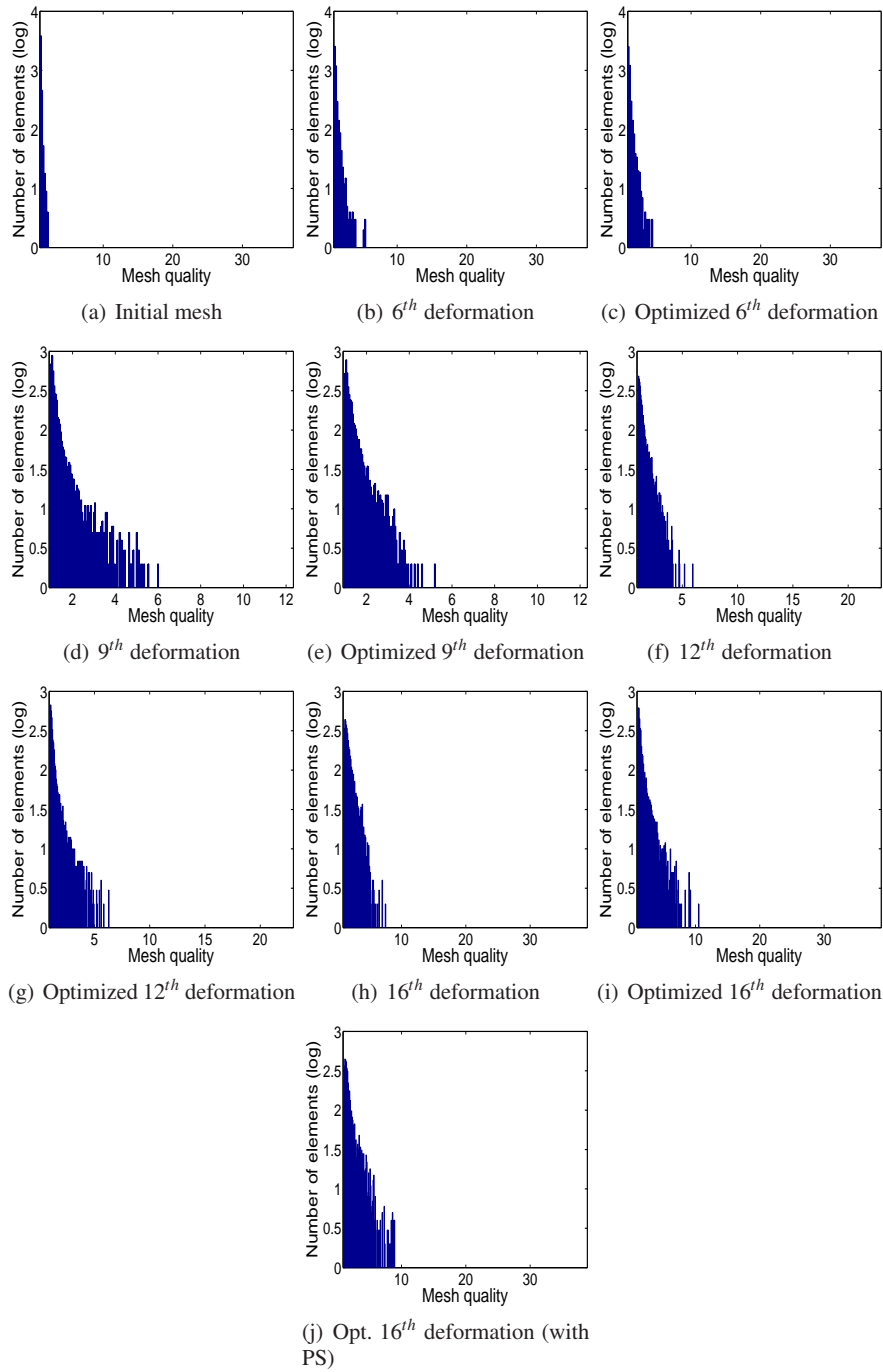


Fig. 18 Inverse mean ratio mesh quality distribution for meshes generated in Simulation 3. Quality distribution for (a) initial mesh, (b) the sixth intermediate mesh, (c) the sixth intermediate mesh after mesh quality improvement was performed, (d) the ninth intermediate mesh after mesh quality improvement was performed, (e) the ninth intermediate mesh after mesh quality improvement was performed, (f) the twelfth intermediate mesh, (g) the twelfth intermediate mesh after mesh quality improvement was performed, (h) the sixteenth intermediate mesh, (i) the sixteenth intermediate mesh after mesh quality improvement was performed, and (j) the sixteenth intermediate mesh after the worst quality element improvement was performed.

Table 4 Inverse mean ratio mesh quality statistics for several meshes used in the simulation. The feasible Newton method [50] implemented in Mesquite [8] was used for average mesh quality improvement. For improving the worst quality of the final mesh, the PS mesh quality improvement algorithm [57] was applied to obtain further improvement.

Mesh	Inverse mean ratio mesh quality				
	min	avg	rms	max	std
Initial mesh	1.00001	1.05380	1.05731	2.3513	0.08604
6 th deformation	1.00000	1.20431	1.50967	36.3021	0.91035
Opt. 6 th deformation	1.00001	1.18070	1.22330	5.5055	0.32000
9 th deformation	1.00005	1.38846	1.51427	11.3377	0.60432
Opt. 9 th deformation	1.00007	1.37350	1.53049	9.1011	0.67520
12 th deformation	1.00043	1.50317	1.65771	21.9930	0.69892
Opt. 12 th deformation	1.00004	1.47862	1.67494	9.0810	0.78682
16 th deformation	1.00061	1.86964	2.24460	14.0210	1.24204
Opt. 16 th deformation	1.00002	1.53606	1.81146	18.4508	0.96015
Opt. 16 th deformation (with PS)	1.00073	1.91943	2.37001	8.9290	1.24050

from 18.4508 to 8.9290, despite the fact that the average mesh quality of the mesh was slightly degraded to 1.91943.

Fig. 18(i) shows that the number of poor mesh quality elements of the sixteenth intermediate mesh increased regardless of performing mesh quality improvement. After the PS algorithm for improving the worst quality element was performed, the number of poor mesh quality elements of the mesh decreased (seen in Fig. 18(j)).

The distances for boundary vertex movement during the deformations are visualized in Fig. 19. The distances were computed by calculating the Euclidean distance between the vertices in each boundary, and not by summing each distance traveled in an intermediate step. The arrows shown in Fig. 19 were generated by connecting two vertices having the same index in each boundary.

When ventricular mesh deformation from pre-treatment to period 1 was performed, the boundary vertices in the lower-left parts of the ventricles moved more than that of the vertices in the other parts of the ventricles. These vertices, which were indexed between 40 to 60, were included in the lower-left parts of the ventricles, and their movement was approximately 80.

The boundary vertex movement from period 1 to period 2 was significantly large. The size of vectors for most of the vertices were larger than that of the previous deformation from pre-treatment to period 1. As can be seen in Fig. 19(d), the distances for most of the vertices were larger than 50 except the vertices indexed between 120 and 130, whose movement was around 10.

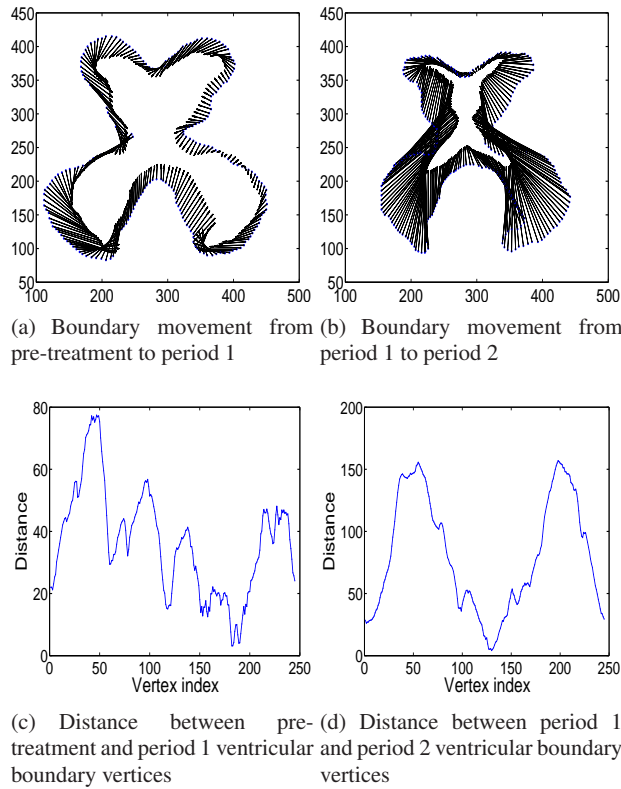


Fig. 19 (a) boundary movement of each vertex from pre-treatment to period 1, (b) boundary movement of each vertex from period 1 to period 2, (c) the distance between the pre-treatment and period 1 vertices, (d) the distance between the period 1 and period 2 vertices.

6 Conclusions and Future Work

We proposed an image-based computational technique for use in tracking the evolution of the brain ventricles in hydrocephalic patients pre- and post-treatment. Such simulations could be used by neurosurgeons in order to design personalized medical treatments for a given patient in that the simulations could be used to determine how a particular treatment may perform on a given patient. Our image-based computational technique is based on a combination of the level set method and the finite element mesh warping (FEMWARP) method [74]. Our computational pipeline involves the pre-processing steps of image denoising and segmentation. The segmented medical images are then used as input to the combined level set/mesh warping algorithm. Next, the level set method is used to predict the next position of the brain ventricles, and the mesh warping method, i.e., FEMWARP, is used to deform

the mesh to the new target. The prediction and deformation steps are performed several times until the final target of the brain ventricles is reached.

Using our approach, we were able to perform three numerical simulations in order to track the evolution of the brain ventricles post-treatment of hydrocephalus via shunt insertion in two patients. In Simulation 1, the ventricular mesh deformation was performed for a case in which the ventricular area decreased while the ventricular shape was preserved. In this case, the ventricular mesh deformation was easy to perform using FEMWARP, and coupling with the level set method was not necessary.

The brain ventricles changed their shapes asymmetrically during their evolution in Simulation 2. Because the deformation of the ventricles was rather large in this case, intermediate mesh deformation steps were designed, and small-step FEMWARP [74] was used in order to deform the mesh. In total, fifteen intermediate deformation steps were performed to track the evolution of the ventricles from pre- to Period 2 of post-treatment. The ninth intermediate mesh matched the ventricular boundary for period 1; the fifteenth mesh matched the ventricular boundary for period 2.

Finally, the level set method was coupled with FEMWARP in Simulation 3 in order to obtain the ventricular boundary vertices in the segmented medical images. Linear interpolation based on the level sets was performed in order to predict the location of the brain ventricles on the intermediate steps. Mesh deformation was again performed via small-step FEMWARP in combination with the predicted target locations. Sixteen intermediate deformation steps were designed, and the ninth intermediate mesh and the sixteenth mesh matched the ventricular boundary for period 1 and period 2, respectively.

Mesh quality improvement was performed on the deformed meshes from all three simulations in order to improve their overall quality. For the sixteenth deformed mesh in Simulation 3, it was also necessary to prove worst element quality mesh improvement in order to further improve the quality of the mesh to an acceptable level for computational purposes.

Our combined level set/mesh warping technique performed semi-automatic ventricular mesh deformation and evolution of the brain ventricles. Future research will focus on fully automating the level set method in its ability to predict the location of the brain ventricles at the next time step. This will require a technique for determining which speed should be applied to each boundary vertex in the level set contour to prescribe its evolution. We will also extend our approach to handle three-dimensional ventricular evolution. It should be noted that a 3D version of FEMWARP is already in existence [74] and can be used for this purpose. In addition, we will extend the FEMWARP method so that it can handle topological changes during the ventricular deformation; mesh adaptation will need to be added to FEMWARP for this purpose. It should be noted that the level set method can already handle topological changes. Finally, it should be noted that FEMWARP is a geometric mesh warping approach. We plan to extend FEMWARP so that it also incorporates brain biomechanics which can be used to predict the evolution of the brain ventricles.

It should also be mentioned that our combined level set/mesh warping method can also be used to analyze other medical conditions for which medical images are acquired. For example, such an approach could also be used to analyze geometric changes in the brain due to normal brain growth or the growth of a tumor, the change in the brain due to a stroke, or the impact of a traumatic injury on the brain. Our approach can also be applied to other medical conditions involving medical images and deformations including several applications in cardiology or orthopaedics.

Acknowledgements The work of the first two authors was funded in part by NSF CAREER Award OCI-1054459; the work of the second author was also funded in part by NSF grant CNS-0720749.

References

1. Adalsteinsson, D., Sethian, J.: A fast level set method for propagating interfaces. *J. Comp. Phys.* **118**, 269–277 (1995)
2. Amato, U., Larobina, M., Antoniadis, A., Alfano, B.: Segmentation of magnetic resonance images through discriminant analysis. *Journal of Neuroscience Methods* **131**, 65–74 (2003)
3. Bah, M., Nair, P., Browne, M.: Mesh morphing for finite element analysis of implant positioning in cementless total hip replacement. *Medical Engineering and Physics* **31**, 1235–1243 (2009)
4. Baker, T.: Mesh movement and metamorphosis. In: *Proc. of the Tenth International Meshing Roundtable*, pp. 387–396. Sandia National Laboratories (2001)
5. Baldwin, M., Langenderfer, J., Rullkoetter, P., Laz, P.: Development of subject-specific and statistical shape models of the knee using an efficient segmentation and mesh-morphing approach. *Computer Methods and Programs in Biomedicine* **97**, 232–240 (2010)
6. Bezdek, J., Hall, L., Clarke, L.: Review of MR segmentation techniques and using pattern recognition. *Medical Physics* **20**, 1033–1048 (1993)
7. Biot, M.: General theory of three-dimensional consolidation. *J. App. Phys* **12**, 155–164 (1941)
8. Brewer, M., Diachin, L., Knupp, P., Leurent, T., Melander, D.: The mesquite mesh quality improvement toolkit. In: *Proc. of the 12th International Meshing Roundtable*, pp. 239–250. Sandia National Laboratories (2003)
9. Bridson, R., Teran, J., Molino, N., Fedkiw, R.: Adaptive physics based tetrahedral mesh generation using level sets. *Engineering with Computers* **21**, 2–18 (2005)
10. Chan, T., Vese, L.: Active contours without edges. *IEEE Transactions on Image Processing* **10** (2001)
11. Choi, J., Kim, D., Kim, S.: Endoscopic surgery for obstructive hydrocephalus. *Yonsei Medical Journal* **40**, 600–607 (1999)
12. de Putter, S., Laffargue, F., Breeuwer, M., van de Vosse, F., Gerritsen, F.: Computational mesh generation for vascular structures with deformable surfaces. *Int. J. CARS* **1**, 39–49 (2006)
13. Di Rocco, C., Massimi, L., Tamburrini, G.: Shunts vs. endoscopic third ventriculostomy in infants: Are there different types and/or rates of complications? A review. *Childs. Nerv. Syst.* **22**, 1573–1589 (2006)
14. Drapaca, C., Tenti, G., Rohlf, K., Sivaloganathan, S.: A quasilinear viscoelastic constitutive equation for the brain: Application to hydrocephalus. *J. Elasticity* **85**, 65–83 (2006)
15. Dyedov, V., Einstein, D., Jiao, X., Kuprat, A., Carsons, J., del Pin, F.: Variational generation of prismatic boundary-layer meshes for biomedical computing. *Int. J. Numer. Meth. Engng* **79**, 907–945 (2009)
16. Egnor, M., Rosiello, A., Zheng, L.: A model of intracranial pulsations. *Pediatr. Neurosurg.* **35**, 284–298 (2001)

17. Evans, L., Spruck, J.: Motion of level sets by mean curvature. *J. Diff. Geometry* **33**, 635–681 (1991)
18. Fillinger, M., Raghavan, M., Marra, S., Cronenwett, J., Kennedy, F.: *In vivo* analysis of mechanical wall stress and abdominal aortic aneurysm risk. *J. Vasc. Surg.* **26**, 589–597 (2002)
19. Fischl, B., Salat, D., Busa, E., Albert, M., Dietrich, M., Haselgrove, C., van der Kouwe, A., Killiany, R., Kennedy, D., Klaveness, S., Montillo, A., Makris, N., Rosen, B., Dale, A.: Whole brain segmentation: Automated labeling of neuroanatomical structures in the human brain. *Neuron* **33**, 341–355 (2002)
20. Frey, P.: Generation and adaptation of computational surface meshes from discrete anatomical data. *Int. J. Numer. Meth. Engng.* **60**, 1049–1074 (2004)
21. Fritz, J., Drapaca, C.: A study of the effect of the pulsatile ventricular pressure in the development of hydrocephalus. In: *Proceedings of the 3rd International Conference in Computational Mechanics and Virtual Engineering COMEC2009*, vol. 1, pp. 254–259 (2009)
22. Gonzalez, R., Woods, R.: *Digital Image Processing*. Addison-Wesley (1992)
23. Hakim, S., Venegas, J., Burton, J.: The physics of the cranial cavity, hydrocephalus and normal pressure hydrocephalus: Mechanical interpretation and mathematical model. *Surg. Neurol.* **5**, 187–210 (1976)
24. Haralick, R., Shapiro, L.: Image segmentation techniques. *Comput. Vis. Graph. Image Proc.* **29**, 100–32 (1985)
25. Held, K., Rota Kops, E., Krause, B., Wells III, W., Kikinis, R., Muller-Gartner, H.: Markov random field segmentation of brain MR images. *IEEE Transactions on Medical Imaging* **16**, 878–886 (1997)
26. Hilton, A., Illingworth, J.: *Marching triangles: Delaunay implicit surface triangulation*. Tech. rep., University of Surrey (1997)
27. Hojjatoleslami, S., Kittler, J.: Region growing: A new approach. *IEEE Transactions on Image Processing* **7**, 1079–1084 (1998)
28. Hojjatoleslami, S., Kruggel, F.: Segmentation of large brain lesions. *IEEE Transactions on Medical Imaging* **20**, 666–669 (2001)
29. Hydrocephalus statistics. See <http://www.ghrforg.org/faq.htm>
30. Ito, Y., Shum, P., Shih, A., Soni, B., Nakahashi, K.: Robust generation of high-quality unstructured meshes on realistic biomedical geometry. *Int. J. Numer. Meth. Engng.* **65**, 943–973 (2006)
31. Johnson, C.: *Numerical Solutions of Partial Differential Equations by the Finite Element Method*. Studentlitteratur (1987)
32. Kaczmarek, M., Subramaniam, R., Neff, S.: The hydromechanics of hydrocephalus: Steady-state solutions for cylindrical geometry. *Bull. Math.Biol.* **59**, 295–323 (1997)
33. Kass, M., Witkin, A., Terzopoulos, D.: Snakes: Active contour models. *International Journal of Computer Vision* **1**, 321–331 (1988)
34. Kellie, G.: Appearances observed in the dissection of two individuals; death from cold and congestion of the brain. *Trans. Med-Chir. Soc. Edinburgh* pp. 1–84 (1824)
35. Langan, D., Modestino, J., Zhang, J.: Cluster validation for unsupervised stochastic model-based image segmentation. *IEEE Trans. Image Process.* **7**, 180–95 (1998)
36. Liu, Y., D’Arceuil, H., He, J., Duggan, M., Gonzalez, G., Pryor, J., de Crespigny, A.: A non-linear mesh-warping technique for correcting brain deformation after stroke. *Magnetic Resonance Imaging* **24**, 1069–1075 (2006)
37. Liu, Y., Foteinos, P., Chernikov, A., Chrisochoides, N.: Multi-tissue mesh generation for brain images. In: *Proc. 19th International Meshing Roundtable*, pp. 367–384 (2010)
38. Lohner, R.: Regridding surface triangulations. *Journal of Computational Physics* **126**, 1–10 (1996)
39. Lorensen, W., Cline, H.: Marching cubes: A high resolution 3D surface construction method. *Comput. Graph.* **21**, 163–169 (1987)
40. Ma, Z., Tavares, J., Jorge, R., Mascarenhas, T.: A review of algorithms for medical image segmentation and their applications to the female pelvic cavity. *Comput Methods Biomech Biomed Engin.* **13**, 235–246 (2010)

41. Magnotta, V., Heckel, D., Andreasen, A., Cizadlo, T., Corson, P., Ehrhardt, J., Yuh, W.: Measurement of brain structures with artificial neural networks: Two- and three-dimensional applications. *Radiology* **211**, 781–90 (1999)
42. Marmarou, A., Shulman, K., Rosende, R.: A nonlinear analysis of the cerebrospinal fluid and intracranial pressure dynamics. *J Neurosurg* **48**, 530–537 (1978)
43. McInerney, T., Tarzopoulos, D.: Deformable medical image analysis: A survey. *Medical Image Analysis* **1**, 91–108 (1996)
44. Mendis, K., Stalnaker, R., Advani, S.: A constitutive relationship for large deformation finite-element modeling of brain-tissue. *J. Biomech. Eng. Trans. ASME* **117**, 279–285 (1995)
45. Miller, K.: Constitutive model of brain tissue suitable for finite element analysis of surgical procedures. *J. Biomech.* **32**, 531–537 (1999)
46. Miller, K., Chinzei, K.: Constitutive modeling of brain tissue: Experiment and theory. *J. Biomech.* **30**, 1115–1121 (1997)
47. Miller, K., Taylor, Z., Wittek, A.: Mathematical models of brain deformation behaviour for computer-integrated neurosurgery. Tech. Rep. ISML/01/2006, The University of Western Australia (2006)
48. Mitich, A., Ayed, I.: Variational and level set methods in image segmentation. Springer Topics in Signal Processing vol.5, Springer (2010)
49. Monro, A.: Observations on Structure and Functions of the Nervous System. Edinburgh: Creech and Johnson (1783)
50. Munson, T.: Mesh shape-quality optimization using the inverse mean-ratio metric. *Math. Program* **110**, 561–590 (2007)
51. Nagashima, T., Tamaki, N., Matsumoto, S., Horwitz, B., Seguchi, Y.: Biomechanics of hydrocephalus: A new theoretical model. *Neurosurg* **21**, 898–904 (1987)
52. Osher, S., Fedkiw, R.: Level set methods: An overview and some recent results. *J. Comp. Phys.* **169**, 463–502 (2001)
53. Osher, S., Fedkiw, R.: Level Set Methods and Dynamic Implicit Surfaces, Applied Mathematical Sciences vol. 153. Springer (2003)
54. Osher, S., Paragolis, N.: Geometric Level Set Methods in Imaging, Vision, and Graphics. Springer (2003)
55. Osher, S., Sethian, J.: Fronts propagating with curvature dependent speed: Algorithms based on Hamilton-Jacobi formulations. *Journal of Computational Physics* **79**, 12–49 (1988)
56. Pal, N., Pal, S.: A review on image segmentation techniques. *Pattern Recognit.* **26**, 1277–94 (1993)
57. Park, J., Shontz, S.: Two derivative-free optimization algorithms for mesh quality improvement. In: Proc. of the 2010 International Conference on Computational Science, pp. 387–396. Amsterdam, Netherlands (2010)
58. Peiro, J., Giordana, S., Griffith, C., Sherwin, S.: High-order algorithms for vascular flow modelling. *Int. J. Numer. Meth. Fluids* **40**, 137–151 (2002)
59. Pena, A., Harris, N., Bolton, M., Czosnyka, M., Pickard, J.: Communicating hydrocephalus: The biomechanics of progressive ventricular enlargement revisited. *Acta Neurochir.* **81**, 59–63 (2002)
60. Peng, D., Merriman, B., Osher, S., Zhao, H., Kang, M.: A PDE-based fast local level set method. *J. Comp. Phys.* **155**, 410–438 (1999)
61. Persson, P.: Mesh generation for implicit geometries. Ph.D. thesis, MIT (2004)
62. Persson, P.: Mesh size functions for implicit geometries and PDE-based gradient limiting. *Engineering with Computers* **22**, 95–109 (2006)
63. Persson, P., Strang, G.: A simple mesh generator in MATLAB. *SIAM Review* **46**, 329–345 (2004)
64. Pham, D., Xu, C., Prince, J.: Current methods in medical image segmentation. *Annu. Rev. Biomed. Eng.* **2**, 315–337 (2000)
65. Quatember, B., Muhlthaler, H.: Generation of CFD meshes from biplane angiograms: An example of image-based mesh generation and simulation. *Appl. Numer. Math.* **46**, 379–397 (2003)

66. Sahoo, P., Soltani, S., Wong, A.: A survey of thresholding techniques. *Comput. Vis. Graph. Image Proc.* **41**, 233–60 (1988)
67. Schmidt, J., Johnson, C., Eason, J., McLeod, R.: Applications of automatic mesh generation and adaptive methods in computational medicine. Springer (1994)
68. Sethian, J.: *Level Set Methods and Fast Marching Methods: Evolving Interfaces in Computational Geometry, Fluid Mechanics, Computer Vision, and Materials Science*. Cambridge Monographs on Applied and Computational Mathematics (1999)
69. Shattuck, D., Mizra, M., Adestiyo, V., Hojatkashani, C., Salamon, G., Narr, K., Poldrack, R., Bilder, R., Toga, A.: Construction of a 3D probabilistic atlas of human cortical structures. *NeuroImage* **39**, 1064–1080 (2008)
70. Shepherd, J., Johnson, C.: Hexahedral mesh generation for biomedical models in SCIRun. *Engineering with Computers* **25**, 97–114 (2009)
71. Shewchuk, J.: Triangle: Engineering a 2D quality mesh generator and delaunay triangular. In: *Applied Computational Geometry: Towards Geometric Engineering*, vol. 1148, pp. 203–222. Springer-Berlin Lecture Notes in Computer Science (1996)
72. Shewchuk, J.: What is a good linear element? Interpolation, conditioning, and quality measures. In: *Proc. of the 11th International Meshing Roundtable*, pp. 115–126. Sandia National Laboratories (2003)
73. Shontz, S.: Numerical methods for problems with moving meshes. Ph.D. thesis, Cornell University (2005)
74. Shontz, S., Vavasis, S.: Analysis of and workarounds for element reversal for a finite element-based algorithm for warping triangular and tetrahedral meshes. *BIT, Numerical Mathematics* **50**, 863–884 (2010)
75. Sigal, I., Hardisty, M., Whyne, C.: Mesh-morphing algorithms for specimen-specific finite element modeling. *Journal of Biomechanics* **41**, 1381–1389 (2008)
76. Sigal, I., Whyne, C.: Mesh morphing and response surface analysis: Quantifying sensitivity of vertebral mechanical behavior. *Annals of Biomedical Engineering* **38**, 41–56 (2010)
77. Sigal, I., Yang, H., Roberts, M., Downs, J.: Morphing methods to parameterize specimenspecific finite element model geometries. *Journal of Biomechanics* **43**, 254–262 (2010)
78. Sivaloganathan, S., Tenti, G., Drake, J.: Mathematical pressure volume models of the cerebrospinal fluid. *Appl. Math. Comput.* **94**, 243–266 (1998)
79. Smillie, A., Sobey, I., Molnar, Z.: A hydroelastic model of hydrocephalus. *J. Fluid Mech.* **539**, 417–443 (2005)
80. Strang, G., Persson, P.: Circuit simulation and moving mesh generation. In: *Proc. of Int. Symp. on Comm. and Inform. Tech. 2004 (ISCIT 2004)* (2004)
81. Szczerba, D., McGregor, R., Szekely, G.: High quality surface mesh generation for multiphysics bio-medical simulations. In: *Proc. of the 2007 International Conference on Computational Science*, vol. 4487, pp. 906–913. Springer Berlin/Heidelberg (2007)
82. Tenti, G., Sivaloganathan, S., Drake, J.: Brain biomechanics: Steady-state consolidation theory of hydrocephalus. *Can. App. Math. Q.* **7**, 111–124 (1999)
83. Tuli, S., Alshail, E., Drake, J.: Third ventriculostomy versus cerebrospinal fluid shunt as a first procedure in pediatric hydrocephalus. *Pediatric Neurosurgery* **30**, 11–15 (1999)
84. Tully, B., Ventikos, Y.: Coupling poroelasticity and CFD for cerebrospinal fluid hydrodynamics. *J. Transactions on Biomedical Engineering* **56**, 1644–1651 (2009)
85. Ulrich, D., van Rietbergen, B., Weinans, H., Ruegsegger, P.: Finite element analysis of trabecular bone structure: A comparison of image-based meshing techniques. *J. Biomech.* **31**, 1187–1192 (1998)
86. Verma, C., Fischer, P., Lee, S., Loth, F.: An all-hex meshing strategy for bifurcation geometries in vascular flow simulation. In: *Proc. of the Fourteenth International Meshing Roundtable*, pp. 11–14. Sandia National Laboratories (2005)
87. Vese, L., Chan, T.: A multiphase level set framework for image segmentation using the Mumford and Shah model. *International Journal of Computer Vision* **50**, 271–293 (2002)
88. Wang, H., Wineman, A.: A mathematical model for the determination of viscoelastic behavior of brain in vivo. i. Oscillatory response. *J. Biomech* **5**, 31–46 (1972)

89. West, J.: Application of the level set method to hydrocephalus: Simulating the motion of the ventricles. Master's thesis, University of Waterloo (2004)
90. Wilkie, K., Drapaca, C., Sivaloganathan, S.: A theoretical study of the effect of ventricular pressure pulsations on the pathogenesis of hydrocephalus. *Appl. Math. Comput.* **215**, 3181–3191 (2010)
91. Withey, D., Koles, Z.: A review of medical image segmentation: Methods and available software. *International Journal of Bioelectromagnetism* **10**, 125–148 (2008)
92. Wu, Y.: Matlab implementation of the chan vese active contour without edges method (2011). See <http://www.mathworks.com/matlabcentral/fileexchange/23445-chan-vese-active-contours-without-edges>
93. Yamakawa, S., Shimada, K.: Converting a tetrahedral mesh to a prism-tetrahedral hybrid mesh for FEM accuracy and efficiency. In: Proc. of the 2008 ACM Symposium on Solid and Physical Modeling, pp. 287–294 (2008)
94. Yu, Z., Holst, M., McCammon, J.: High-fidelity geometric modeling for biomedical applications. *Finite elements in analysis and design* **44**, 715–723 (2008)
95. Zachariah, S., Sanders, J., Turkiyyah, G.: Automated hexahedral mesh generation from biomedical image data: Applications in limb prosthetics. *IEEE Transactions on Rehabilitation Engineering* **4**, 91–102 (1996)